

1

2 The ANTsX ecosystem for mapping the 3 mouse brain

4 Nicholas J. Tustison^{1,✉}, Min Chen², Fae N. Kronman³, Jeffrey T. Duda², Clare Gamlin⁴,
5 Mia G. Tustison⁵, Michael Kunst⁴, Rachel Dalley⁴, Staci Sorenson⁴, Quanxin Wang⁴, Lydia
6 Ng⁴, Yongsoo Kim³, and James C. Gee^{2,✉}

7 ¹Department of Radiology and Medical Imaging, University of Virginia, Charlottesville, VA

8 ²Department of Radiology, University of Pennsylvania, Philadelphia, PA

9 ³Department of Neuroscience and Experimental Therapeutics, Penn State University, Hershey, PA

10 ⁴Allen Institute for Brain Science, Seattle, WA

11 ⁵Santiago High School, Corona, CA

12

13 ✉ Corresponding authors:

14

15 Nicholas J. Tustison, DSc

16 Department of Radiology and Medical Imaging

17 University of Virginia

18 ntustison@virginia.edu

19

20 James C. Gee, PhD

21 Department of Radiology

22 University of Pennsylvania

23 gee@upenn.edu

²⁴ **Abstract**

²⁵ Large-scale efforts by the BRAIN Initiative Cell Census Network (BICCN) are generating a
²⁶ comprehensive reference atlas of cell types in the mouse brain. A key challenge in this effort
²⁷ is mapping diverse datasets, acquired with varied imaging, tissue processing, and profiling
²⁸ methods, into shared coordinate frameworks. Here, we present modular mapping pipelines
²⁹ developed using the Advanced Normalization Tools Ecosystem (ANTsX) to align MERFISH
³⁰ spatial transcriptomics and high-resolution fMOST morphology data to the Allen Common
³¹ Coordinate Framework (CCFv3), and developmental MRI and LSFM data to the Devel-
³² opmental CCF (DevCCF). Simultaneously, we introduce two novel methods: 1) a velocity
³³ field-based approach for continuous interpolation across developmental timepoints, and 2)
³⁴ a deep learning framework for automated brain parcellation using minimally annotated and
³⁵ publicly available data. All workflows are open-source and reproducible. We also provide
³⁶ general guidance for selecting appropriate strategies across modalities, enabling researchers
³⁷ to adapt these tools to new data.

³⁸ Introduction

³⁹ Over the past decade, there have been significant advancements in mesoscopic single-cell
⁴⁰ analysis of the mouse brain. It is now possible to track single neurons¹, observe whole-
⁴¹ brain developmental changes at cellular resolution², associate brain regions with genetic
⁴² composition³, and locally characterize neural connectivity⁴. These scientific achievements
⁴³ have been propelled by high-resolution profiling and imaging techniques that enable sub-
⁴⁴ micron, multimodal, 3D characterizations of whole mouse brains. Among these are micro-
⁴⁵ optical sectioning tomography^{5,6}, tissue clearing methods^{1,7}, spatial transcriptomics^{8,9}, and
⁴⁶ single-cell genomic profiling¹⁰, each offering expanded specificity and resolution for cell-level
⁴⁷ brain analysis.

⁴⁸ Recent efforts by the NIH BRAIN Initiative have mobilized large-scale international collabora-
⁴⁹ tions to create a comprehensive reference database of mouse brain structure and function.
⁵⁰ The BRAIN Initiative Cell Census Network has aggregated over 40 multimodal datasets from
⁵¹ more than 30 research groups¹¹, many of which are registered to standardized anatomical co-
⁵² ordinate systems to support integrated analysis. Among the most widely used of these frame-
⁵³ works is the Allen Mouse Brain Common Coordinate Framework (CCFv3)¹². Other CCFs
⁵⁴ include modality-specific references^{13–15} and developmental atlases^{16,17} that track structural
⁵⁵ change across time.

⁵⁶ Mouse brain mapping challenges

⁵⁷ Robust mapping of cell type data into CCFs is essential for integrative analysis of morphology,
⁵⁸ connectivity, and molecular identity. However, each modality poses unique challenges. For
⁵⁹ example, differences in tissue processing, imaging protocols, and anatomical completeness
⁶⁰ often introduce artifacts such as distortion, tearing, holes, and signal dropout^{18–23}. Inten-
⁶¹ sity differences and partial representations of anatomy can further complicate alignment.
⁶² Also, while alternative strategies for mapping single-cell spatial transcriptomic data exist
⁶³ (e.g., gene expression-based models such as Tangram²⁴) this work focuses on image-based
⁶⁴ anatomical alignment to common coordinate frameworks using spatially resolved reference

65 images. Given this diversity specialized strategies are often needed to address the unique,
66 modality-specific challenges.

67 Existing mapping solutions fall into three broad categories. The first includes integrated
68 processing platforms that provide users with mapped datasets (e.g., Allen Brain Cell
69 Atlas²⁵, Brain Architecture Portal²⁶, OpenBrainMap²⁷, and Image and Multi-Morphology
70 Pipeline²⁸). These offer convenience and high-quality curated data, but limited gener-
71 alizability and customization. The second category involves highly specialized pipelines
72 tailored to specific modalities such as histology^{29–31}, magnetic resonance imaging (MRI)^{32–34},
73 microCT^{35,36}, light sheet fluorescence microscopy (LSFM)^{37,38}, flourescence micro-optical
74 sectioning tomography (fMOST)^{15,39}, and spatial transcriptomics, including multiplexed
75 error-robust fluorescence *in situ* hybridization (MERFISH)^{40–42}. While effective, these
76 solutions often require extensive engineering effort to adapt to new datasets or modal-
77 ities. Finally, general-purpose toolkits such as elastix⁴³, Slicer3D⁴⁴, and the Advanced
78 Normalization Tools Ecosystem (ANTsX)⁴⁵ have all been applied to mouse brain mapping
79 scenarios. These toolkits support modular workflows that can be flexibly composed from
80 reusable components, offering a powerful alternative to rigid, modality-specific solutions.
81 However, their use often requires familiarity with pipeline modules, parameter tuning, and
82 tool-specific conventions which can limit adoption.

83 Building on this third category, we describe a set of modular, ANTsX-based pipelines specif-
84 ically tailored for mapping diverse mouse brain data into standardized anatomical frame-
85 works. These include two new pipelines: a velocity field-based interpolation model that
86 enables continuous transformations across developmental timepoints of the DevCCF, and a
87 template-based deep learning pipeline for whole brain segmentation (i.e., brain extraction)
88 and structural anatomical regional labeling of the brain (i.e., brain parcellation) requiring
89 minimal annotated data. In addition, we include two modular pipelines for aligning MER-
90 FISH and fMOST datasets to the Allen CCFv3. While the MERFISH dataset was previously
91 published as part of earlier BICCN efforts⁴⁶, the full image processing and registration work-
92 flow had not been described in detail until now. The fMOST workflow, by contrast, was
93 developed internally to support high-resolution morphology mapping and has not been pre-

94 viously published in any form. Both pipelines were built using ANTsX tools, adapted for
95 collaborative use with the Allen Institute, and are now released as fully reproducible, open-
96 source workflows to support reuse and extension by the community. To facilitate broader
97 adoption, we also provide general guidance for customizing these strategies across imaging
98 modalities and data types. We first introduce key components of the ANTsX toolkit, which
99 provide a basis for all of the mapping workflows described here, and then detail the specific
100 contributions made in each pipeline.

101 **The Advanced Normalization Tools Ecosystem (ANTsX)**

102 The Advanced Normalization Tools Ecosystem (ANTsX) has been used in a number of
103 applications for mapping mouse brain data as part of core processing steps in various
104 workflows^{31,46–49}, particularly its pairwise, intensity-based image registration capabilities⁵⁰
105 and bias field correction⁵¹. Historically, ANTsX development is based on foundational ap-
106 proaches to image mapping^{52–54}, especially in the human brain, with key contributions such
107 as the Symmetric Normalization (SyN) algorithm⁵⁰. It has been independently evaluated
108 in diverse imaging domains including multi-site brain MRI⁵⁵, pulmonary CT⁵⁶, and multi-
109 modal brain tumor registration⁵⁷. More recent contributions for mouse-specific applications
110 showcase multimodal template generation¹⁶ and anatomy-aware registration ANTsX func-
111 tionality.

112 Beyond registration, ANTsX provides functionality for template generation⁵⁸, segmentation⁵⁹,
113 preprocessing^{51,60}, and deep learning⁴⁵. It has demonstrated strong performance in consen-
114 sus labeling⁶¹, brain tumor segmentation⁶², and cardiac motion estimation⁶³. Built on the
115 Insight Toolkit (ITK)⁶⁴, ANTsX benefits from open-source contributions while supporting
116 continued algorithm evaluation and innovation. In the context of mouse brain data, ANTsX
117 provides a robust platform for developing modular pipelines to map diverse imaging modal-
118 ities into CCFs. These tools span multiple classes of mapping problems: cross-modality
119 image registration, landmark-driven alignment, temporal interpolation across developmental
120 stages, and deep learning-based segmentation. As such, they also serve as illustrative case
121 studies for adapting ANTsX tools to other use cases. We describe both shared infrastructure

122 and targeted strategies adapted to the specific challenges of each modality. This paper
123 highlights usage across distinct BICCN projects such as spatial transcriptomic data from
124 MERFISH, structural data from fMOST, and multimodal developmental data from LSFM
125 and MRI.

126 **Novel ANTsX-based open-source contributions**

127 We introduce two novel contributions to ANTsX developed as part of collaborative efforts
128 in creating the Developmental Common Coordinate Framework (DevCCF)¹⁶. First, we
129 present an open-source velocity field-based interpolation framework for continuous map-
130 ping across the sampled embryonic and postnatal stages of the DevCCF atlas¹⁶. This
131 functionality enables biologically plausible interpolation between timepoints via a time-
132 parameterized diffeomorphic velocity model⁶⁵, inspired by previous work⁶⁶. Second, we
133 present a deep learning pipeline for structural parcellation of the mouse brain from mul-
134 timodal MRI data. This includes two novel components: 1) a template-derived brain ex-
135 traction model using augmented data from two ANTsX-derived template datasets^{67,68}, and
136 2) a template-derived parcellation model trained on DevCCF P56 labelings mapped from
137 the AllenCCFv3. This pipeline demonstrates how ANTsX tools and public resources can be
138 leveraged to build robust anatomical segmentation pipelines with minimal annotated data.
139 We independently evaluate this framework using a longitudinal external dataset⁶⁹, demon-
140 strating generalizability across specimens and imaging protocols. All components are openly
141 available through the R and Python ANTsX packages, with general-purpose functionality
142 documented in a reproducible, cross-platform tutorial (<https://tinyurl.com/antsxtutorial>).
143 Code specific to this manuscript, including scripts to reproduce the novel contributions
144 and all associated evaluations, is provided in a dedicated repository (<https://github.com/>
145 [ntustison/ANTsXMouseBrainMapping](https://github.com/ntustison/ANTsXMouseBrainMapping)). Additional tools for mapping spatial transcriptomic
146 (MERFISH) and structural (fMOST) data to the AllenCCFv3 are separately available at
147 (<https://github.com/dontminchenit/CCFAlignmentToolkit>).

148 **Results**

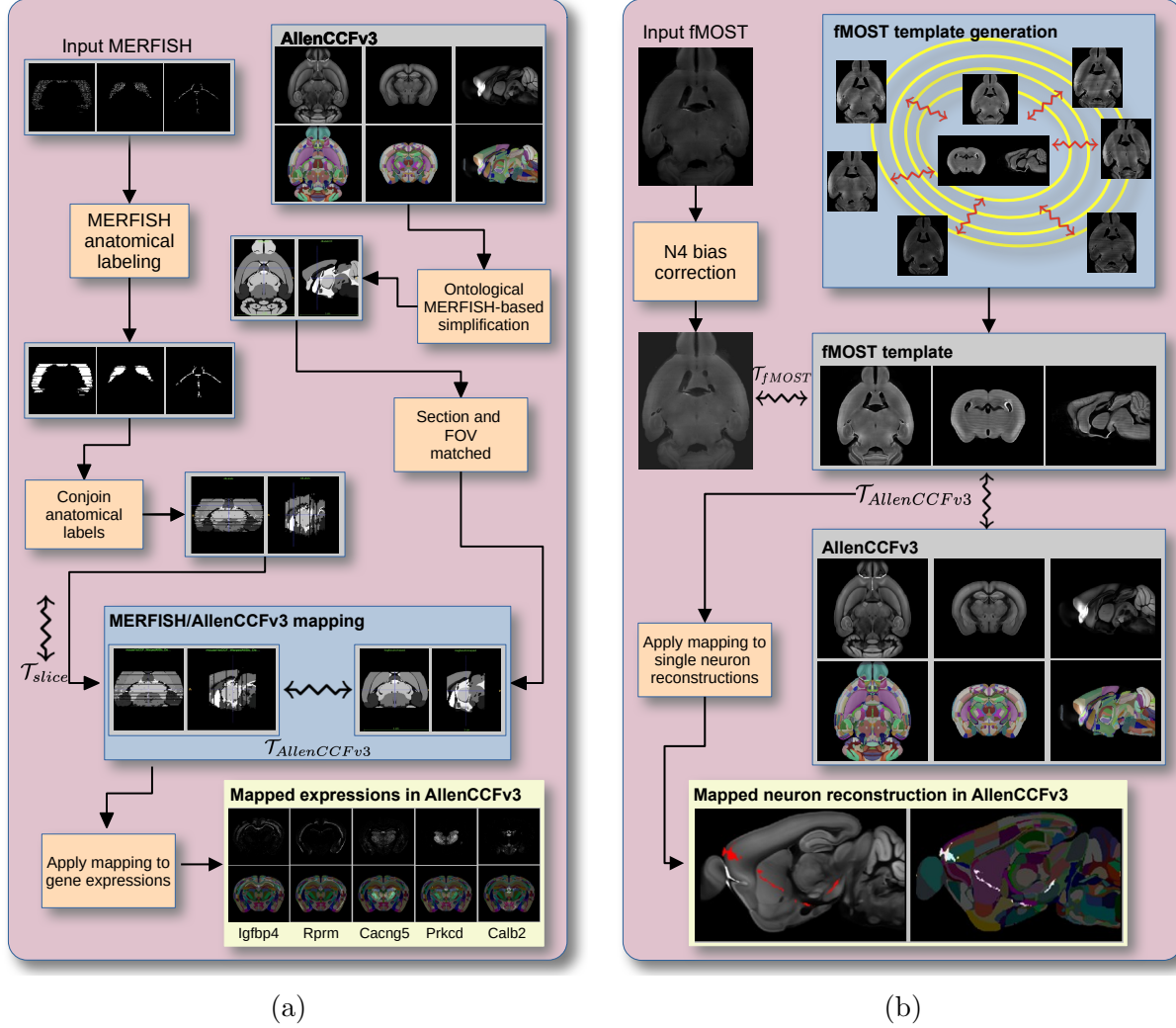


Figure 1: Diagram of the two ANTsX-based pipelines for mapping (a) MERFISH and (b)fMOST data into the space of AllenCCFv3. Each generates the requisite transforms to map individual images to the CCF.

149 **Mapping multiplexed error-robust fluorescence *in situ* hybridization (MERFISH)**

151 We developed an ANTsX-based pipeline to map spatial transcriptomic MERFISH data into
 152 the AllenCCFv3 (Figure 1(a)). This approach was used in recent efforts to create a high-
 153 resolution transcriptomic atlas of the mouse brain⁴⁶. The pipeline maps spatial gene ex-

¹⁵⁴ pression patterns from MERFISH onto anatomical labels in the AllenCCFv3. It includes
¹⁵⁵ MERFISH-specific preprocessing steps such as section reconstruction, label generation from
¹⁵⁶ spatial transcriptomic maps, and anatomical correspondence mapping. Alignment proceeds
¹⁵⁷ in two stages: 1) 3D affine registration and section matching of the AllenCCFv3 to the
¹⁵⁸ MERFISH data, and 2) linear + deformable 2D section-wise alignment between matched
¹⁵⁹ MERFISH and atlas slices. These transformations are concatenated to produce a complete
¹⁶⁰ mapping from each MERFISH data to AllenCCFv3.

¹⁶¹ MERFISH imaging was performed on cryosectioned brains from C57BL/6 mice using previ-
¹⁶² ously described protocols⁴⁶. Brains were placed into an optimal cutting temperature (OCT)
¹⁶³ compound (Sakura FineTek 4583) stored at -80°. The fresh frozen brain was sectioned at
¹⁶⁴ 10 μm on Leica 3050 S cryostats at intervals of 200 μm to evenly cover the brain. A set
¹⁶⁵ of 500 genes was selected to distinguish \sim 5200 transcriptomic clusters. Raw MERSCOPE
¹⁶⁶ data were decoded using Vizgen software (v231). Cell segmentation was performed us-
¹⁶⁷ ing Cellpose^{70,71} based on DAPI and PolyT stains which was propagated to adjacent slices
¹⁶⁸ across z-planes. Each MERFISH cell was assigned a transcriptomic identity by mapping to
¹⁶⁹ a scRNA-seq reference taxonomy.

¹⁷⁰ Alignment quality was evaluated iteratively by an expert anatomist, guided by expected
¹⁷¹ gene-marker correspondences to AllenCCFv3 regions. As previously reported⁴⁶, further as-
¹⁷² sessment of the alignment showed that, of the 554 terminal regions (gray matter only in
¹⁷³ the AllenCCFv3), only seven small subregions did not contain cells from the MERFISH
¹⁷⁴ dataset post registration: frontal pole, layer 1 (FRP1), FRP2/3, FRP5; accessory olfactory
¹⁷⁵ bulb, glomerular layer (AOBgl); accessory olfactory bulb, granular layer (AOBgr); accessory
¹⁷⁶ olfactory bulb, mitral layer (AOBmi); and accessory supraoptic group (ASO). A broader dis-
¹⁷⁷ cussion of evaluation design choices and evaluation rationale is included in the Discussion.

¹⁷⁸ Mapping fluorescence micro-optical sectioning tomography
¹⁷⁹ (fMOST) data

¹⁸⁰ We also constructed a pipeline for mapping fMOST images to the AllenCCFv3 using
¹⁸¹ ANTsX (Figure 1(b)). The approach leverages a modality-specific average fMOST at-
¹⁸² las as an intermediate target, adapted from previous work in human and mouse brain
¹⁸³ mapping^{12,15,16,58,72–75}. The atlas was constructed from 30 fMOST images selected to
¹⁸⁴ capture representative variability in anatomical shape and image intensity across the pop-
¹⁸⁵ ulation. Preprocessing includes cubic B-spline downsampling to match the 25 μm isotropic
¹⁸⁶ AllenCCFv3 resolution, stripe artifact suppression using a 3D notch filter implemented
¹⁸⁷ with SciPy’s frequency-domain filtering tools, and N4 bias field correction⁵¹. A one-time,
¹⁸⁸ annotation-driven alignment registers the fMOST atlas to AllenCCFv3 using landmark-
¹⁸⁹ based registration of key structures. This canonical mapping is then reused. New fMOST
¹⁹⁰ specimens are first aligned to the fMOST atlas using standard intensity-based registration,
¹⁹¹ and the concatenated transforms yield full spatial normalization to the AllenCCFv3. This
¹⁹² same mapping can be applied to neuron reconstructions to facilitate population-level
¹⁹³ analysis of morphology and spatial distribution.

¹⁹⁴ fMOST imaging was performed on 55 mouse brains with sparse transgenic labeling of neuron
¹⁹⁵ populations^{76,77} using the high-throughput fMOST platform^{78,79}. Voxel resolution was $0.35 \times$
¹⁹⁶ $0.35 \times 1.0 \mu\text{m}^3$. Two imaging channels were acquired: GFP-labeled neuron morphology
¹⁹⁷ (green), and propidium iodide counterstaining for cytoarchitecture (red). Alignment was
¹⁹⁸ performed using the red channel for its greater contrast, though multi-channel mapping is
¹⁹⁹ also supported.

²⁰⁰ The canonical mapping from the fMOST atlas to AllenCCFv3 was evaluated using both
²⁰¹ quantitative and qualitative approaches. Dice similarity coefficients were computed between
²⁰² corresponding anatomical labels in the fMOST atlas and AllenCCFv3 following registra-
²⁰³ tion. These labels were manually annotated or adapted from existing atlas segmentations.
²⁰⁴ Representative Dice scores included: whole brain (0.99), caudate putamen (0.97), fimbria
²⁰⁵ (0.91), posterior choroid plexus (0.93), anterior choroid plexus (0.96), optic chiasm (0.77),
²⁰⁶ and habenular commissure (0.63). In addition to these quantitative assessments, each regis-

207 tered fMOST specimen was evaluated qualitatively. An expert anatomist reviewed alignment
208 accuracy and confirmed structural correspondence. Neuron reconstructions from individual
209 brains were also transformed into AllenCCFv3 space, and their trajectories were visually
210 inspected to confirm anatomical plausibility and preservation of known projection patterns.
211 A broader discussion of evaluation design choices and evaluation rationale is included in the
212 Discussion.

213 Continuously mapping the DevCCF developmental trajectory

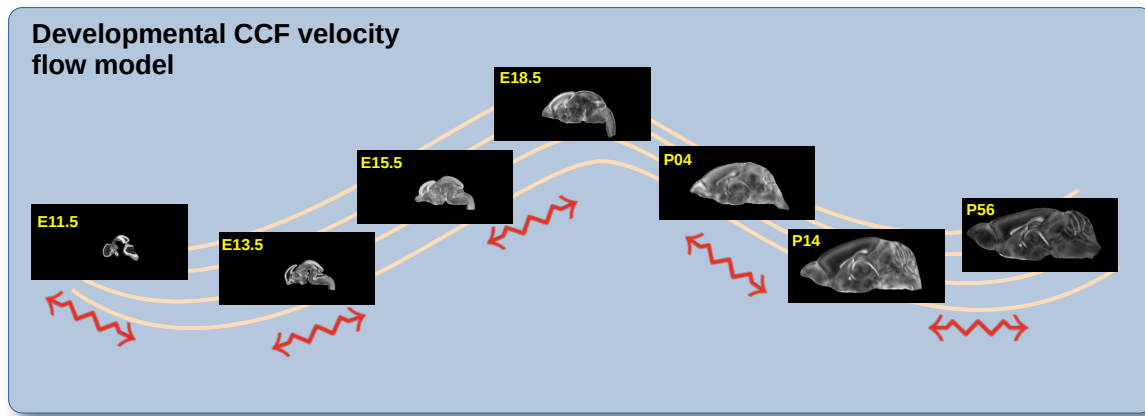


Figure 2: The spatial transformation between any two time points within the continuous DevCCF longitudinal developmental trajectory is available through the use of ANTsX functionality for generating a velocity flow model.

214 The DevCCF is an openly accessible resource for the mouse brain research community¹⁶,
215 comprising symmetric, multi-modal MRI and LSFM templates generated using the ANTsX
216 framework⁵⁸. It spans key stages of mouse brain development (E11.5, E13.5, E15.5, E18.5,
217 P4, P14, and P56) and includes structural labels defined by a developmental ontology.
218 The DevCCF was constructed in coordination with the AllenCCFv3 to facilitate integra-
219 tion across atlases and data types.

220 Although this collection provides broad developmental coverage, its discrete sampling
221 limits the ability to model continuous transformations across time. To address this, we
222 developed a velocity flow-based modeling approach that enables anatomically plausible,

223 diffeomorphic transformations between any two continuous time points within the De-
 224 vCCF range. Unlike traditional pairwise interpolation, which requires sequential warping
 225 through each intermediate stage, this model, defined by a time-varying velocity field
 226 (i.e., a smooth vector field defined over space and time that governs the continuous
 227 deformation of an image domain), allows direct computation of deformations between
 228 any two time points in the continuum which improves smoothness and enables flexi-
 229 ble spatiotemporal alignment. This functionality is implemented in both ANTsR and
 230 ANTsPy (see `ants.fit_time_varying_transform_to_point_sets(...)`) and integrates
 231 seamlessly with existing ANTsX workflows. The velocity field is represented as a 4D
 232 ITK image where each voxel stores the x,y,z components of motion at a given time
 233 point. Integration of the time-varying velocity field uses uses 4th order Runge-Kutta
 234 (`ants.integrate_velocity_field(...)`)⁸⁰.

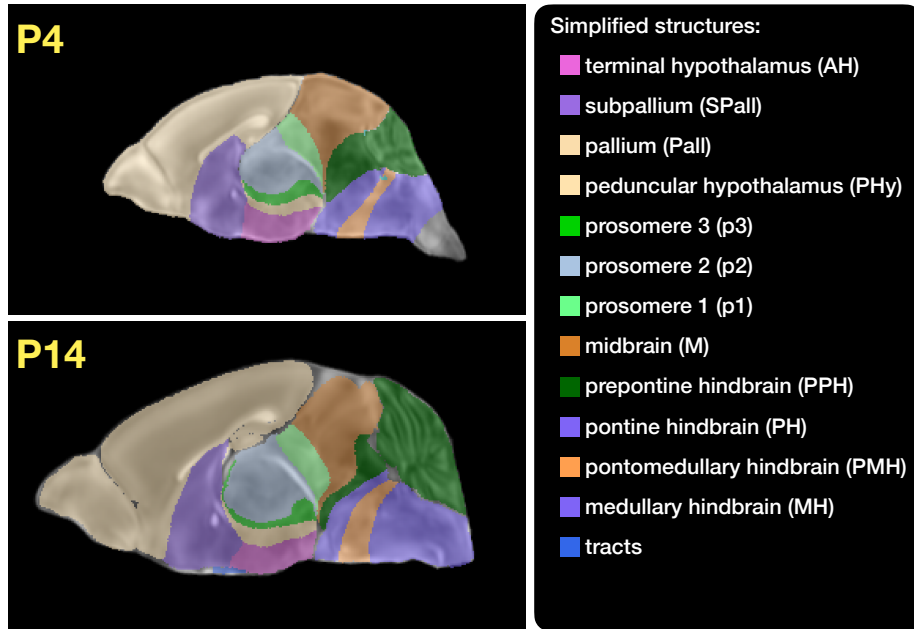


Figure 3: Annotated regions representing common labels across developmental stages, shown for both P4 and P14.

235 Each DevCCF template includes over 2,500 labeled anatomical regions, with spatial reso-
 236 lutions ranging from 31.5 to 50 μm . For the velocity flow modeling task, we identified a
 237 common set of 26 bilateral regions (13 per hemisphere) that were consistently labeled across
 238 all timepoints. These regions span major developmental domains including the pallium, sub-

239 pallium, midbrain, prosomeres, hypothalamus, hindbrain subregions, and key white matter
240 tracts (Figure 3).

241 Prior to velocity field optimization, all templates were rigidly aligned to the DevCCF P56
242 template using the centroids of these common label sets. Pairwise correspondence be-
243 tween adjacent timepoints was then computed using ANTsX’s multi-metric registration via
244 `ants.registration(...)`. Instead of performing intensity-based multi-label registration di-
245 rectly, we constructed 24 binary label masks per atlas pair (one per structure) and optimized
246 alignment using the mean squares similarity metric with the SyN transform⁵⁰.

247 To generate the point sets for velocity field optimization, we sampled both boundary (con-
248 tour) and interior (region) points from the P56 labels and propagated them to each devel-
249 opmental stage using the learned pairwise transforms. Contours were sampled at 10% of
250 available points and regions at 1%, yielding 173,303 total points per atlas ($N_{contour} = 98,151$;
251 $N_{region} = 75,152$). Boundary points were assigned double weight during optimization to
252 emphasize anatomical boundary correspondence.

253 The velocity field was optimized using the seven corresponding point sets and their associated
254 weights. The field geometry was defined at [256, 182, 360] with 11 integration points at 50
255 μm resolution, yielding a compressed velocity model of ~ 2 GB. This resolution balanced
256 accuracy and computational tractability while remaining portable. All data and code are
257 publicly available in the accompanying GitHub repository.

258 To normalize temporal spacing, we assigned scalar values in [0, 1] to each template. Given
259 the nonlinear spacing in postnatal development, we applied a logarithmic transform to the
260 raw time values prior to normalization. Within this logarithmic temporal transform, P56
261 was assigned a span of 28 postnatal days to reflect known developmental dynamics (i.e., in
262 terms of modeling the continuous deformation, the morphological changes between Day 28
263 and Day 56 are insignificant). This improved the temporal distribution of integration points
264 (Figure 4, right panel).

265 Optimization was run for a maximum of 200 iterations using a 2020 iMac (3.6 GHz 10-Core
266 Intel Core i9, 64 GB RAM), with each iteration taking ~ 6 minutes. During each iteration,
267 the velocity field was updated across all 11 integration points by computing regularized

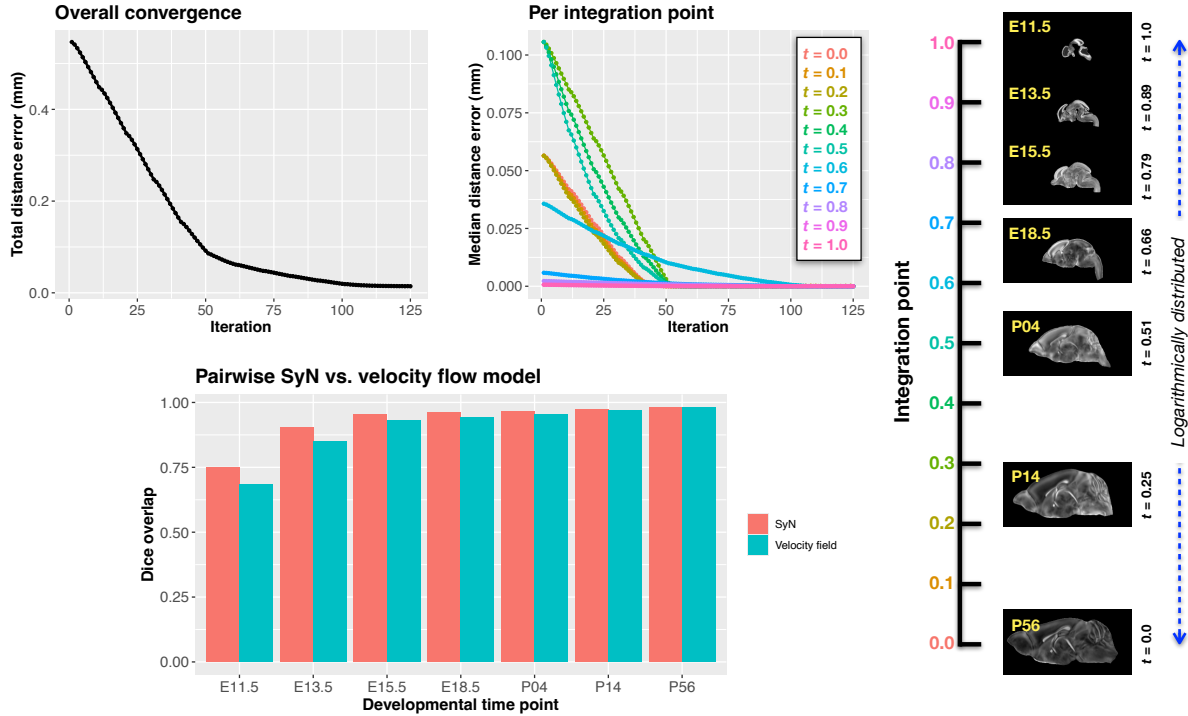


Figure 4: Convergence and evaluation of the velocity flow model across the DevCCF developmental trajectory. (Top left) Total displacement error over iterations. (Top right) Median displacement error per integration point across the optimization timeline, spanning embryonic (E11.5) to postnatal (P56) stages. (Bottom) Dice similarity scores comparing region-level label overlap between: (1) conventional pairwise SyN registration and (2) velocity flow-based deformation, across intermediate timepoints. Using region-based pairwise registration with SyN as a performance upper bound, the velocity flow model achieves comparable accuracy while also enabling smooth, continuous deformation across the full developmental continuum.

displacement fields between warped point sets at adjacent time slices. Updates were applied using a step size of $\delta = 0.2$. Convergence was assessed via average displacement error across all points, with final convergence achieved after ~ 125 iterations (Figure 4, left panel). Median errors across integration points also trended toward zero, albeit at varying rates. To benchmark performance, we compared the velocity model’s region-based alignment to traditional pairwise registration using SyN, a widely used diffeomorphic algorithm. The velocity model achieved comparable Dice scores at sampled timepoints while additionally offering smooth interpolation across the entire developmental trajectory. Once optimized, the velocity field enables the computation of diffeomorphic transformations between any pair of continuous time points within the DevCCF developmental range. Fig-

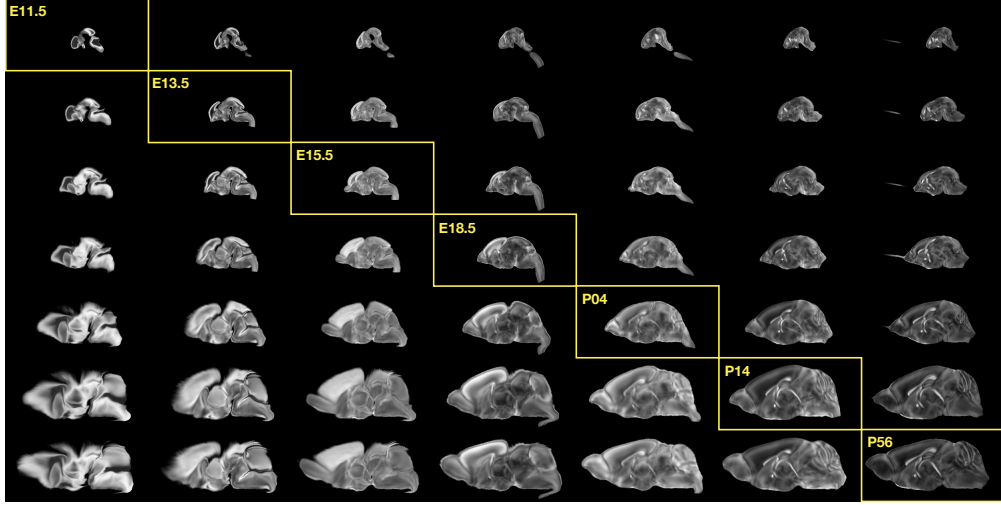


Figure 5: Mid-sagittal visualization of DevCCF templates warped to every other time point. Each row is a reference space; each column is a warped input. Diagonal entries show original templates.

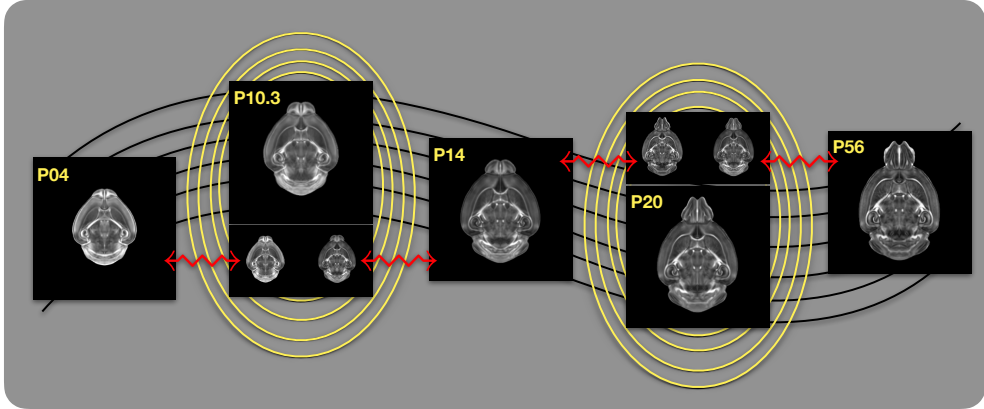


Figure 6: Example of generating “virtual” DevCCF templates at intermediate time points (e.g., P10.3, P20) by warping adjacent stages to a shared time and averaging using ANTsX.

Figure 5 illustrates cross-warping between all DevCCF stages using the velocity flow model. In addition to facilitating flexible alignment between existing templates, the model also supports the synthesis of virtual templates at intermediate, unsampled developmental stages. As shown in Figure 6, we demonstrate the creation of virtual age templates (e.g., P10.3 and P20) by warping adjacent developmental atlases to a target timepoint and constructing an averaged representation using ANTsX’s template-building functionality.

All usage examples, scripts, and supporting data for full reproducibility are publicly available in the associated codebase.

286 **Automated structural labeling of the mouse brain**

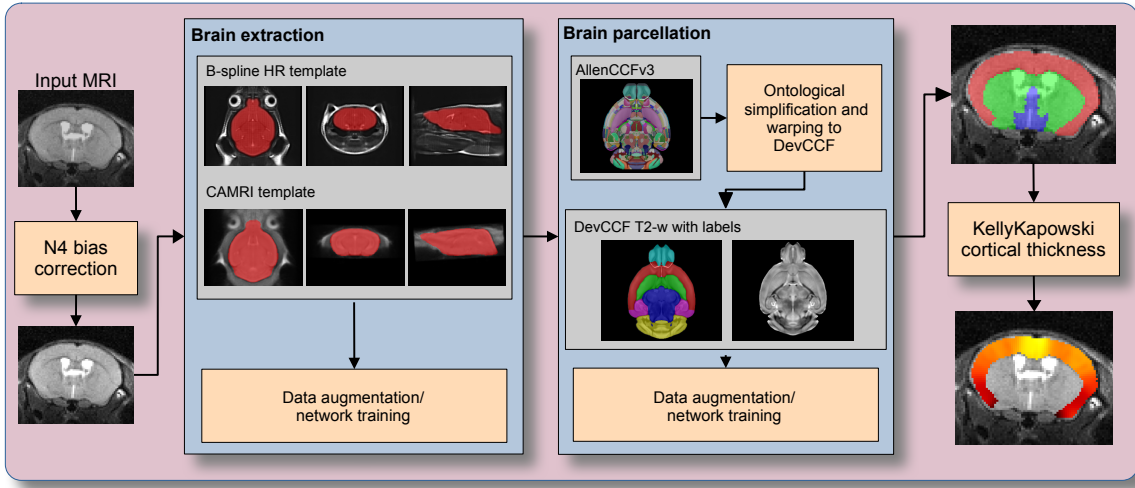


Figure 7: The mouse brain cortical labeling pipeline integrates two deep learning components for brain extraction and anatomical region segmentation. Both networks rely heavily on data augmentation applied to templates constructed from open datasets. The framework also supports further refinement or alternative label sets tailored to specific research needs. Possible applications include voxelwise cortical thickness estimation.

287 Structural labeling strategies for the mouse brain are essential for understanding the organization
 288 and function of the murine nervous system⁸¹. By dividing the brain into anatomically
 289 or functionally defined regions, researchers can localize biological processes, relate regional
 290 features to behavior, or quantify spatial variation in gene expression patterns^{82,83}. While
 291 deep learning techniques have yielded robust segmentation and labeling tools for the hu-
 292 man brain (e.g., SynthSeg⁸⁴, ANTsXNet⁴⁵), analogous development for mouse data (e.g.,
 293 MEMOS⁸⁵) has been limited. Mouse neuroimaging often presents unique challenges, such
 294 as highly anisotropic sampling, that complicate transfer of existing tools. At the same time,
 295 high resolution resources like the AllenCCFv3 and DevCCF provide reference label sets that
 296 can serve as training data. We demonstrate how ANTsX can be used to construct a full
 297 structural labeling pipeline for the mouse brain (Figure 7), including both whole brain seg-
 298 mentation (i.e., brain extraction) and the subsequent template-based region segmentation.
 299 To develop a general-purpose mouse brain extraction model, we constructed whole-head
 300 templates from two publicly available T2-weighted datasets. The first dataset, from the

301 Center for Animal MRI (CAMRI) at the University of North Carolina at Chapel Hill⁶⁷,
302 includes 16 isotropic MRI volumes acquired at $0.16 \times 0.16 \times 0.16$ mm³ resolution. The second
303 dataset⁶⁸ comprises 88 specimens acquired in three orthogonal 2D views (coronal, axial,
304 sagittal) at 0.08×0.08 mm³ in-plane resolution with 0.5 mm slice thickness. These orthogonal
305 2D acquisitions were reconstructed into high-resolution 3D volumes using a B-spline fitting
306 algorithm⁸⁶. Using this synthesized dataset and the CAMRI images, we created two ANTsX-
307 based population templates⁵⁸, each paired with a manually delineated brain mask. These
308 served as the basis for training an initial template-based brain extraction model. Deep
309 learning training of the network employed aggressive data augmentation strategies, including
310 bias field simulation, histogram warping, random spatial deformation, noise injection, and
311 anisotropic resampling. This enabled the model to generalize beyond the two templates.
312 The initial model was released through ANTsXNet and made publicly available.

313 Subsequent community use led to further improvements. A research group applying the
314 tool to their own ex vivo T2-weighted mouse brain data contributed a third template and
315 associated mask (acquired at 0.08 mm isotropic resolution). Incorporating this into the
316 training data improved robustness and accuracy to an independent dataset and extended
317 the model's generalizability. The refined model is distributed through ANTsPyNet via
318 `antspynet.mouse_brain_extraction(...)`.

319 The AllenCCFv3 atlas and its hierarchical ontology, along with the DevCCF, provide a strong
320 foundation for developing region-wise anatomical labeling models for multi-modal mouse
321 brain imaging. Using the `allensdk` Python library, we generated a coarse segmentation
322 scheme by grouping anatomical labels into six major regions: cerebral cortex, cerebral nuclei,
323 brainstem, cerebellum, main olfactory bulb, and hippocampal formation. These labels were
324 mapped onto the P56 T2-weighted DevCCF template to serve as training targets. We trained
325 a 3D U-net-based segmentation network using this template and the same augmentation
326 strategies described for brain extraction. The model is publicly available via ANTsXNet
327 (`antspynet.mouse_brain_parcellation(...)`) and supports robust anatomical labeling
328 across diverse imaging geometries and contrasts. The inclusion of aggressive augmentation,
329 including simulated anisotropy, enables the model to perform well even on thick-slice input

330 data. Internally, the model reconstructs isotropic probability and label maps, facilitating
 331 downstream morphometric analyses. For example, this network integrates with the ANTsX
 332 cortical thickness estimation pipeline (`antspynet.mouse_cortical_thickness(...)`) to
 333 produce voxelwise cortical thickness maps, even when applied to anisotropic or limited-
 334 resolution mouse brain data.

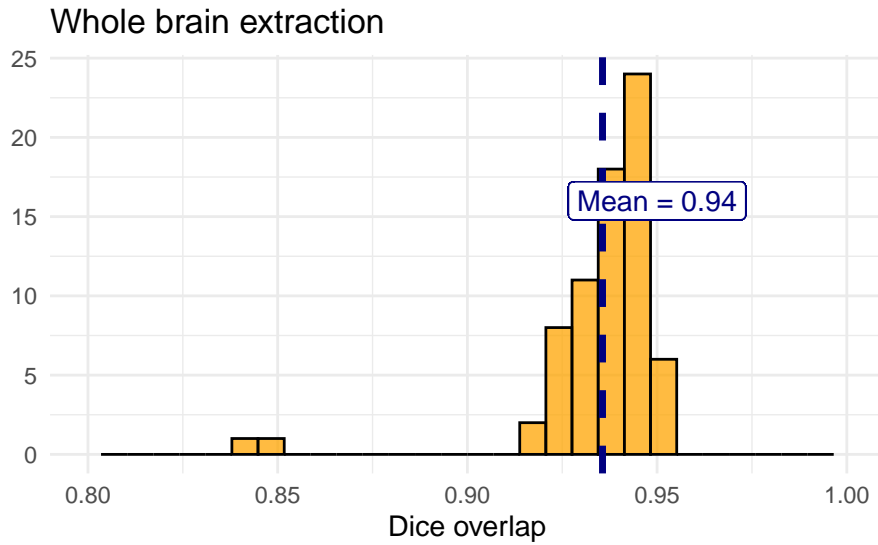
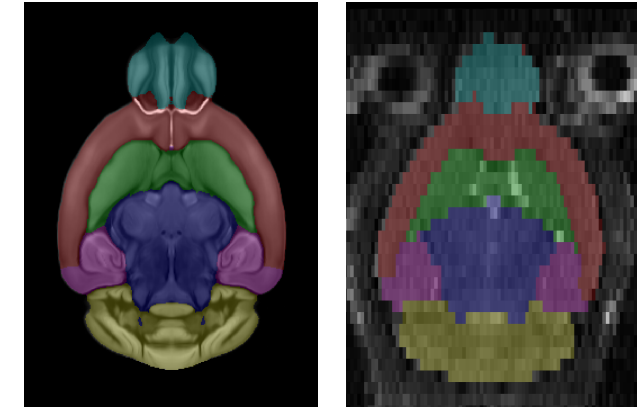


Figure 8: Evaluation of the ANTsX mouse brain extraction on an independent, publicly available dataset consisting of 12 specimens \times 7 time points = 84 total images. Dice overlap comparisons with the user-generated brain masks provide good agreement with the automated results from the brain extraction network.

335 For evaluation, we used an additional publicly available dataset⁶⁹ that is completely inde-
 336 pendent from the data used in training the brain extraction and parcellation networks. Data
 337 includes 12 specimens each imaged at seven time points (Day 0, Day 3, Week 1, Week 4,
 338 Week 8, Week 20) with in-house-generated brain masks (i.e., produced by the data providers)
 339 for a total of 84 images. Spacing is anistropic with an in-plane resolution of $0.1 \times 0.1 \text{ mm}^2$
 340 and a slice thickness of 0.5 mm.

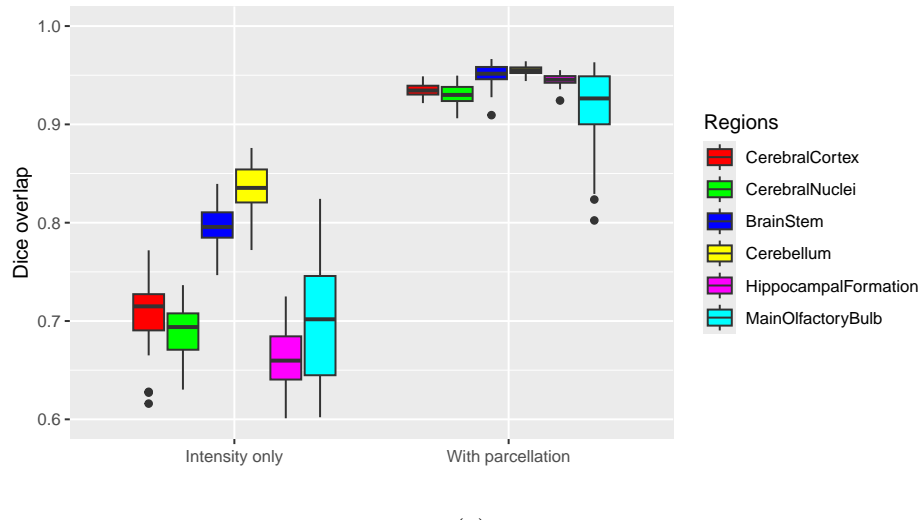
341 Figure 8 summarizes the whole-brain overlap between manually segmented reference masks
 342 and the predicted segmentations for all 84 images in the evaluation cohort. The proposed
 343 network demonstrates excellent performance in brain extraction across a wide age range. To
 344 further assess the utility of the parcellation network, we used the predicted labels to guide
 345 anatomically informed registration to the AllenCCFv3 atlas using ANTsX multi-component



(a)

(b)

Normalization to AllenCCFv3



(c)

Figure 9: Evaluation of the ANTsX deep learning–based mouse brain parcellation on a diverse MRI cohort. (a) T2-weighted DevCCF P56 template with the six-region parcellation: cerebral cortex, nuclei, brain stem, cerebellum, main olfactory bulb, and hippocampal formation. (b) Example segmentation result from a representative subject (NR5, Day 0) using the proposed deep learning pipeline. (c) Dice overlap scores across the full evaluation cohort ($n = 84$), comparing anatomical alignment achieved via registration using intensity alone versus registration guided by the predicted parcellation. Dice values were computed using manually segmented labels transformed to AllenCCFv3 space.

³⁴⁶ registration, and compared this to intensity-only registration (Figure 9). While intensity-
³⁴⁷ based alignment performs reasonably well, incorporating the predicted parcellation signifi-
³⁴⁸cantly improves regional correspondence. Dice scores shown in Figure 9(c) were computed
³⁴⁹ using manually segmented labels transformed to AllenCCFv3 space.

350 **Discussion**

351 The diverse mouse brain cell type profiles gathered through BICCN and associated efforts
352 provide a rich multi-modal resource to the research community. However, despite significant
353 progress, optimal leveraging of these valuable resources remains an ongoing challenge. A
354 central component to data integration is accurately mapping novel cell type data into com-
355 mon coordinate frameworks (CCFs) for subsequent processing and analysis. To meet these
356 needs, tools for mapping mouse brain data must be both broadly accessible and capable of
357 addressing challenges unique to each modality. In this work, we described modular ANTsX-
358 based pipelines developed to support three distinct BICCN efforts encompassing spatial
359 transcriptomic, morphological, and developmental data. We demonstrated how a flexible
360 image analysis toolkit like ANTsX can be tailored to address specific modality-driven con-
361 straints by leveraging reusable, validated components.

362 As part of collaborative efforts with the Allen Institute for Brain Science and the broader
363 BICCN initiative, we developed two modular pipelines for mapping MERFISH and fMOST
364 datasets to the AllenCCFv3. These workflows were designed to accommodate the spe-
365 cific requirements of high-resolution transcriptomic and morphological data while leveraging
366 reusable components from the ANTsX ecosystem. The MERFISH pipeline incorporates
367 preprocessing and registration steps tailored to known anatomical and imaging artifacts in
368 multiplexed spatial transcriptomic data. While the general mapping strategy is applicable
369 to other sectioned histological datasets, these refinements demonstrate how general-purpose
370 tools can be customized to meet the demands of specialized modalities. The fMOST work-
371 flow, in contrast, emphasizes reusability and consistency across large datasets. It introduces
372 an intermediate, canonical fMOST atlas to stabilize transformations to the AllenCCFv3,
373 reducing the need for repeated manual alignment and enabling standardized mapping of
374 single-neuron reconstructions to a common coordinate framework.

375 Evaluation of both workflows followed established QA/QC protocols used at the Allen In-
376 stitute, emphasizing biologically meaningful criteria such as expected gene-marker align-
377 ment (MERFISH) and accurate reconstruction of neuronal morphology (fMOST). These
378 domain-informed assessments, also used in prior large-scale mapping projects⁴⁶, prioritize

379 task-relevant accuracy over other possible benchmarks such as Dice coefficients or landmark
380 distances. While formal quantitative scores were not reported for these specific pipelines,
381 they both demonstrate reliable, expert-validated performance in collaborative contexts. Ad-
382 dditional documentation and evaluation commentary are available in the updated CCFAlign-
383 mentToolkit GitHub repository.

384 For developmental data, we introduced a velocity field-based model for continuous interpo-
385 lation between discrete DevCCF timepoints. Although the DevCCF substantially expands
386 coverage of developmental stages relative to prior atlases, temporal gaps remain. The ve-
387 locity model enables spatio-temporal transformations within the full developmental interval
388 and supports the generation of virtual templates at unsampled ages. This functionality is
389 built using ANTsX components for velocity field optimization and integration, and offers
390 a novel mechanism for interpolating across the non-linear developmental trajectory of the
391 mouse brain. Such interpolation has potential utility for both anatomical harmonization and
392 longitudinal analyses. Interestingly, long-range transformations (e.g., P56 to E11.5) revealed
393 anatomy evolving in plausible ways yet sometimes diverging from known developmental pat-
394 terns (e.g., hippocampal shape changes) reflecting the input data and offering insight into
395 temporal gaps. These behaviors could assist future efforts to determine which additional
396 time points would most improve spatiotemporal coverage.

397 We also introduced a template-based deep learning pipeline for mouse brain extraction and
398 parcellation using aggressive data augmentation. This approach is designed to reduce the
399 reliance on large annotated training datasets, which remain limited in the mouse imaging
400 domain. Evaluation on independent data demonstrates promising generalization, though
401 further refinement will be necessary. As with our human-based ANTsX pipelines, failure
402 cases can be manually corrected and recycled into future training cycles. Community con-
403 tributions are welcomed and encouraged, providing a pathway for continuous improvement
404 and adaptation to new datasets.

405 The ANTsX ecosystem offers a powerful foundation for constructing scalable, reproducible
406 pipelines for mouse brain data analysis. Its modular design and multi-platform support
407 enable researchers to develop customized workflows without extensive new software devel-

⁴⁰⁸ opment. The widespread use of ANTsX components across the neuroimaging community
⁴⁰⁹ attests to its utility and reliability. As a continuation of the BICCN program, ANTsX is
⁴¹⁰ well positioned to support the goals of the BRAIN Initiative Cell Atlas Network (BICAN)
⁴¹¹ and future efforts to extend these mapping strategies to the human brain.

412 **Methods**

413 The following methods are all available as part of the ANTsX ecosystem with analogous
414 elements existing in both ANTsR (ANTs in R) and ANTsPy (ANTs in Python), under-
415 pinned by a shared ANTs/ITK C++ core. Most development for the work described was
416 performed using ANTsPy. For equivalent functionality in ANTsR, we refer the reader to the
417 comprehensive ANTsX tutorial: <https://tinyurl.com/antsxtutorial>.

418 **General ANTsX utilities**

419 Although focused on distinct data types, the three pipelines presented in this work share
420 common components that address general challenges in mapping mouse brain data. These
421 include correcting image intensity artifacts, denoising, spatial registration, template gen-
422 eration, and visualization. Table 1 provides a concise summary of the relevant ANTsX
423 functionality.

424 **Preprocessing: bias field correction and denoising.** Standard preprocessing steps in
425 mouse brain imaging include correcting for spatial intensity inhomogeneities and reducing im-
426 age noise, both of which can impact registration accuracy and downstream analysis. ANTsX
427 provides implementations of widely used methods for these tasks. The N4 bias field correction
428 algorithm⁵¹, originally developed in ANTs and contributed to ITK, mitigates artifactual, low-
429 frequency intensity variation and is accessible via `ants.n4_bias_field_correction(...)`.
430 Patch-based denoising⁶⁰ has been implemented as `ants.denoise_image(...)`.

431 **Image registration.** ANTsX includes a robust and flexible framework for pairwise
432 and groupwise image registration⁸⁰. At its core is the SyN algorithm⁵⁰, a symmetric
433 diffeomorphic model with optional B-spline regularization⁶⁶. In ANTsPy, registration
434 is performed via `ants.registration(...)` using preconfigured parameter sets (e.g.,
435 `antsRegistrationSyNQuick[s]`, `antsRegistrationSyN[s]`) suitable for different imaging
436 modalities and levels of computational demand. Resulting transformations can be applied
437 to new images with `ants.apply_transforms(...)`.

438 **Template generation.** ANTsX supports population-based template generation through it-
439 erative pairwise registration to an evolving estimate of the mean shape and intensity reference
440 space across subjects⁵⁸. This functionality was used in generating the DevCCF templates¹⁶.
441 The procedure, implemented as `ants.build_template(...)`, produces average images in
442 both shape and intensity by aligning all inputs to a common evolving template.

443 **Visualization.** To support visual inspection and quality control, ANTsPy provides flexible
444 image visualization with `ants.plot(...)`. This function enables multi-slice and multi-
445 orientation rendering with optional overlays and label maps.

446 Mapping fMOST data to AllenCCFv3

447 **Preprocessing.** Mapping fMOST data into the AllenCCFv3 presents unique challenges due
448 to its native ultra-high resolution and imaging artifacts common to the fMOST modality.
449 Each fMOST image can exceed a terabyte in size, with spatial resolutions far exceeding
450 those of the AllenCCFv3 ($25\text{ }\mu\text{m}$ isotropic). To reduce computational burden and prevent
451 resolution mismatch, each fMOST image is downsampled using cubic B-spline interpolation
452 via `ants.resample_image(...)` to match the template resolution.

453 Stripe artifacts (i.e., periodic intensity distortions caused by nonuniform sectioning or il-
454 lumination) are common in fMOST and can mislead deformable registration algorithms.
455 These were removed using a custom 3D notch filter (`remove_stripe_artifact(...)`) im-
456 plemented in the `CCFAlignmentToolkit` using SciPy frequency domain filtering. The filter
457 targets dominant stripe frequencies along a user-specified axis in the Fourier domain. In
458 addition, intensity inhomogeneity across sections, often arising from variable staining or
459 illumination, was corrected using N4 bias field correction.

460 **Template-based spatial normalization.** To facilitate reproducible mapping, we first
461 constructed a contralaterally symmetric average template from 30 fMOST brains and their
462 mirrored counterparts using ANTsX template-building tools. Because the AllenCCFv3 and
463 fMOST data differ substantially in both intensity contrast and morphology, direct deformable
464 registration between individual fMOST brains and the AllenCCFv3 was insufficiently robust.

465 Instead, we performed a one-time expert-guided label-driven registration between the aver-
466 age fMOST template and AllenCCFv3. This involved sequential alignment of seven manually
467 selected anatomical regions: 1) brain mask/ventricles, 2) caudate/putamen, 3) fimbria, 4)
468 posterior choroid plexus, 5) optic chiasm, 6) anterior choroid plexus, and 7) habenular com-
469 missure which were prioritized to enable coarse-to-fine correction of shape differences. Once
470 established, this fMOST-template-to-AllenCCFv3 transform was reused for all subsequent
471 specimens. Each new fMOST brain was then registered to the average fMOST template
472 using intensity-based registration, followed by concatenation of transforms to produce the
473 final mapping into AllenCCFv3 space.

474 **Mapping neuron projections.** A key advantage of fMOST imaging is its ability to support
475 single neuron projection reconstruction across the entire brain⁷⁷. Because these reconstruc-
476 tions are stored as 3D point sets aligned to the original fMOST volume, we applied the same
477 composite transform used for image alignment to the point data using ANTsX functional-
478 ity. This enables seamless integration of cellular morphology data into AllenCCFv3 space,
479 facilitating comparative analyses across specimens.

480 Mapping MERFISH data to AllenCCFv3

481 **Preprocessing.** MERFISH data are acquired as a series of 2D tissue sections, each com-
482 prising spatially localized gene expression measurements at subcellular resolution. To enable
483 3D mapping to the AllenCCFv3, we first constructed anatomical reference images by aggre-
484 gating the number of detected transcripts per voxel across all probes within each section.
485 These 2D projections were resampled to a resolution of $10 \mu m \times 10 \mu m$ to match the in-plane
486 resolution of the AllenCCFv3.

487 Sections were coarsely aligned using manually annotated dorsal and ventral midline points,
488 allowing initial volumetric reconstruction. However, anatomical fidelity remained limited by
489 variation in section orientation, spacing, and tissue loss. To further constrain alignment and
490 enable deformable registration, we derived region-level anatomical labels directly from the
491 gene expression data.

492 **Label creation.** To assign region labels to the MERFISH data, we use a cell type cluster-
493 ing approach previously detailed⁴⁶. In short, manually dissected scRNAseq data was used
494 to establish the distribution of cell types present in each of the following major regions:
495 cerebellum, CTXsp, hindbrain, HPF, hypothalamus, isocortex, LSX, midbrain, OLF, PAL,
496 sAMY, STRd, STRv, thalamus and hindbrain. Clusters in the scRNA-seq dataset were then
497 used to assign similar clusters of cell types in the MERFISH data to the regions they are
498 predominantly found in the scRNA-seq data. To account for clusters that were found at
499 low frequency in regions outside its main region we calculated for each cell its 50 nearest
500 neighbors in physical space and reassigned each cell to the region annotation dominating its
501 neighborhood.

502 **Section matching via global alignment.** A major challenge was compensating for oblique
503 cutting angles and non-uniform section thickness, which distort the anatomical shape and
504 spacing of the reconstructed volume. Rather than directly warping the MERFISH data
505 into atlas space, we globally aligned the AllenCCFv3 to the MERFISH coordinate system.
506 This was done via an affine transformation followed by resampling of AllenCCFv3 sections
507 to match the number and orientation of MERFISH sections. This approach minimizes
508 interpolation artifacts in the MERFISH data and facilitates one-to-one section matching.

509 **Landmark-driven deformable alignment.** We used a 2.5D approach for fine alignment
510 of individual sections. In each MERFISH slice, deformable registration was driven by sequen-
511 tial alignment of anatomical landmarks between the label maps derived from MERFISH and
512 AllenCCFv3. A total of nine regions, including isocortical layers 2/3, 5, and 6, the striatum,
513 hippocampus, thalamus, and medial/lateral habenula, were registered in an empirically de-
514 termined order. After each round, anatomical alignment was visually assessed by an expert,
515 and the next structure was selected to maximize improvement in the remaining misaligned
516 regions.

517 The final transform for each section combined the global affine alignment and the per-
518 structure deformable registrations. These were concatenated to generate a 3D mapping from
519 the original MERFISH space to the AllenCCFv3 coordinate system. Once established, the
520 composite mapping enables direct transfer of gene-level and cell-type data from MERFISH

521 into atlas space, allowing integration with other imaging and annotation datasets.

522 DevCCF velocity flow transformation model

523 The Developmental Common Coordinate Framework (DevCCF)¹⁶ provides a discrete set of
524 age-specific templates that temporally sample the developmental trajectory. To model this
525 biological progression more continuously, we introduce a velocity flow-based paradigm for in-
526 ferring diffeomorphic transformations between developmental stages. This enables anatomi-
527 cally plausible estimation of intermediate templates or mappings at arbitrary timepoints
528 between the E11.5 and P56 endpoints of the DevCCF. Our approach builds on established
529 insights from time-varying diffeomorphic registration⁶⁵, where a velocity field governs the
530 smooth deformation of anatomical structures over time. Importantly, the framework is ex-
531 tensible and can naturally accommodate additional timepoints for the potential expansion
532 of the DevCCF.

533 **Point sampling and region correspondence.** We first coalesced the anatomical labels
534 across the seven DevCCF templates (E11.5, E13.5, E15.5, E18.5, P4, P14, P56) into 26
535 common structures that could be consistently identified across development. These include
536 major brain regions such as the cortex, cerebellum, hippocampus, midbrain, and ventricles.
537 For each successive pair of templates, we performed multi-label deformable registration us-
538 ing ANTsX to generate forward and inverse transforms between anatomical label volumes.
539 From the P56 space, we randomly sampled approximately 1e6 points within and along the
540 boundaries of each labeled region and propagated them through each pairwise mapping step
541 (e.g., P56 → P14, P14 → P4, . . . , E13.5 → E11.5). This procedure created time-indexed
542 point sets tracing the spatial evolution of each region.

543 **Velocity field fitting.** Using these point sets, we fit a continuous velocity field over develop-
544 mental time using a generalized B-spline scattered data approximation method⁸⁶. The field
545 was parameterized over a log-scaled time axis to ensure finer temporal resolution during early
546 embryonic stages, where morphological changes are most rapid. Optimization proceeded for
547 approximately 125 iterations, minimizing the average Euclidean norm between transformed
548 points at each step. Ten integration points were used to ensure numerical stability. The

549 result is a smooth, differentiable vector field that defines a diffeomorphic transform between
550 any two timepoints within the template range.

551 **Applications and availability.** This velocity model can be used to estimate spa-
552 tial transformations between any pair of developmental stages—even those for which
553 no empirical template exists—allowing researchers to create interpolated atlases, align
554 new datasets, or measure continuous structural changes. It also enables developmental
555 alignment of multi-modal data (e.g., MRI to LSFM) by acting as a unifying spatiotem-
556 poral scaffold. The underlying components for velocity field fitting and integration
557 are implemented in ITK, and the complete workflow is accessible in both ANTsPy
558 (`ants.fit_time_varying_transform_to_point_sets(...)`) and ANTsR. In addition
559 the availability of the DevCCF use case, self-contained examples and usage tutorials are
560 provided in our public codebase.

561 Automated brain extraction and parcellation with ANTsXNet

562 To support template-based deep learning approaches for structural brain extraction and par-
563 cellation, we implemented dedicated pipelines using the ANTsXNet framework. ANTsXNet
564 comprises open-source deep learning libraries in both Python (ANTsPyNet) and R (ANTsR-
565 Net) that interface with the broader ANTsX ecosystem and are built on TensorFlow/Keras.
566 Our mouse brain pipelines mirror existing ANTsXNet tools for human imaging but are
567 adapted for species-specific anatomical variation, lower SNR, and heterogeneous acquisition
568 protocols.

569 Deep learning training setup

570 All network-based approaches were implemented using a standard U-net⁸⁷ architecture and
571 hyperparameters previously evaluated in ANTsXNet pipelines for human brain imaging⁴⁵.
572 This design follows the ‘no-new-net’ principle⁸⁸, which demonstrates that a well-configured,
573 conventional U-net can achieve robust and competitive performance across a wide range of
574 biomedical segmentation tasks with little to no architectural modifications from the original.

575 Both networks use a 3D U-net architecture implemented in TensorFlow/Keras, with five
576 encoding/decoding levels and skip connections. The loss function combined Dice and cate-
577 gorical cross-entropy terms. Training used a batch size of 4, Adam optimizer with an initial
578 learning rate of 2e-4, and early stopping based on validation loss. Training was performed on
579 an NVIDIA DGX system ($4 \times$ Tesla V100 GPUs, 256 GB RAM). Model weights and prepro-
580 cessing routines are shared across ANTsPyNet and ANTsRNet to ensure reproducibility and
581 language portability. For both published and unpublished trained networks available through
582 ANTsXNet, all training scripts and data augmentation generators are publicly available at
583 <https://github.com/ntustison/ANTsXNetTraining>.

584 **Data augmentation.** Robust data augmentation was critical to generalization across scan-
585 ners, contrast types, and resolutions. We applied both intensity- and shape-based augmen-
586 tation strategies:

587 • *Intensity augmentations:*

- 588 – Gaussian, Poisson, and salt-and-pepper noise:
589 `ants.add_noise_to_image(...)`
- 590 – Simulated intensity inhomogeneity via bias field modeling⁵¹:
591 `antspynet.simulate_bias_field(...)`
- 592 – Histogram warping to simulate contrast variation⁸⁹:
593 `antspynet.histogram_warp_image_intensities(...)`

594 • *Shape augmentations:*

- 595 – Random nonlinear deformations and affine transforms:
596 `antspynet.randomly_transform_image_data(...)`
- 597 – Anisotropic resampling across axial, sagittal, and coronal planes:
598 `ants.resample_image(...)`

599 **Brain extraction**

600 We originally trained a mouse-specific brain extraction model on two manually masked
601 T2-weighted templates, generated from public datasets^{67,68}. One of the templates was
602 constructed from orthogonal 2D acquisitions using B-spline-based volumetric synthesis via
603 `ants.fit_bspline_object_to_scattered_data(...)`. Normalized gradient magnitude
604 was used as a weighting function to emphasize boundaries during reconstruction⁸⁶.

605 This training strategy provides strong spatial priors despite limited data by leveraging high-
606 quality template images and aggressive augmentation to mimic population variability. Dur-
607 ing the development of this work, the network was further refined through community en-
608 gagement. A user from a U.S.-based research institute applied this publicly available (but
609 then unpublished) brain extraction tool to their own mouse MRI dataset. Based on feedback
610 and iterative collaboration with the ANTsX team, the model was retrained and improved to
611 better generalize to additional imaging contexts. This reflects our broader commitment to
612 community-driven development and responsiveness to user needs across diverse mouse brain
613 imaging scenarios.

614 The final trained network is available via ANTsXNet through the function
615 `antspynet.mouse_extraction(...)`. Additionally, both template/mask pairs are
616 accessible via ANTsXNet. For example, one such image pair is available via:

- 617 • Template:

618 `antspynet.get_antsxnet_data("bsplineT2MouseTemplate")`

- 619 • Brain mask:

620 `antspynet.get_antsxnet_data("bsplineT2MouseTemplateBrainMask")`

621 **Brain parcellation**

622 For brain parcellation, we trained a 3D U-net model using the DevCCF P56 T2-weighted
623 template and anatomical segmentations derived from AllenCCFv3. This template-based
624 training strategy enables the model to produce accurate, multi-region parcellations without
625 requiring large-scale annotated subject data.

626 To normalize intensity across specimens, input images were preprocessed using rank-based
627 intensity normalization (`ants.rank_intensity(...)`). Spatial harmonization was achieved
628 through affine and deformable alignment of each extracted brain to the P56 template prior
629 to inference. In addition to the normalized image input, the network also receives prior
630 probability maps derived from the atlas segmentations, providing additional spatial context.
631 This general parcellation deep learning framework has also been applied in collaboration
632 with other groups pursuing related but distinct projects. In one case, a model variant was
633 adapted for T2-weighted MRI using an alternative anatomical labeling scheme; in another,
634 a separate model was developed for serial two-photon tomography (STPT) with a different
635 parcellation set. All three models are accessible through a shared interface in ANTsXNet:
636 `antspynet.mouse_brain_parcellation(...)`. Ongoing work is further extending this ap-
637 proach to embryonic mouse brain data. These independent efforts reflect broader community
638 interest in adaptable parcellation tools and reinforce the utility of ANTsXNet as a platform
639 for reproducible, extensible deep learning workflows.

640 Evaluation and reuse

641 To assess model generalizability, both the brain extraction and parcellation networks were
642 evaluated on an independent longitudinal dataset comprising multiple imaging sessions with
643 varied acquisition parameters⁶⁹. Although each label or imaging modality required re-
644 training, the process was streamlined by the reusable ANTsX infrastructure enabled by
645 rapid adaptation with minimal overhead. These results illustrate the practical benefits of a
646 template-based, low-shot strategy and modular deep learning framework. All trained mod-
647 els, associated training scripts, and supporting resources are openly available and designed
648 for straightforward integration into ANTsX workflows.

649 **Data Availability**

650 The following datasets were used in this study and are publicly available:

- 651 • **Allen Common Coordinate Framework (AllenCCFv3):** Available from the Allen
652 Institute for Brain Science at <https://atlas.brain-map.org/atlas>.
- 653 • **Developmental Common Coordinate Framework (DevCCF) MRI and LSFM**
654 datasets: Publicly available via the Kim Lab <https://kimlab.io/home/projects/>
655 [DevCCF/index.html](#).
- 656 • **MERFISH spatial transcriptomics data:** Previously published⁴⁶ [https://portal.](https://portal.brain-map.org)
657 [brain-map.org](#).
- 658 • **Developmental datasets for brain extraction and segmentation:**
 - 659 – High-resolution MRI data of brain C57BL/6 and BTBR mice in three different
660 anatomical views: <https://data.mendeley.com/datasets/dz9x23fttt/1>.
 - 661 – CAMRI Mouse Brain Data: [https://openneuro.org/datasets/ds002868/versions/](https://openneuro.org/datasets/ds002868/versions/1.0.1)
662 [1.0.1](#)
- 663 • **Evaluation dataset for brain extraction and segmentation:** A longitudinal
664 microstructural MRI dataset in healthy C57Bl/6 mice at 9.4 Tesla <https://www.fdr-dfdr.ca/repo/dataset/9ea832ad-7f36-4e37-b7ac-47167c0001c1>.
- 666 • **ANTsXNet-pretrained templates and models:** Available through ANTsPy at
667 <https://github.com/ANTsX/ANTsPyNet>.

668 **Code Availability**

669 All processing pipelines and supporting code are openly available at:

- 670 • <https://github.com/ntustison/ANTsXMouseBrainMapping> (DevCCF velocity model
671 and deep learning parcellation). Also contains the text, scripts, and data to reproduce
672 the manuscript (including figures).
- 673 • <https://github.com/dontminchenit/CCFAlignmentToolkit> (MERFISH and fMOST
674 workflows)

675 **References**

- 676 1. Keller, P. J. & Ahrens, M. B. Visualizing whole-brain activity and development at
the single-cell level using light-sheet microscopy. *Neuron* **85**, 462–83 (2015).
- 677 2. La Manno, G. *et al.* Molecular architecture of the developing mouse brain. *Nature*
596, 92–96 (2021).
- 678 3. Wen, L. *et al.* Single-cell technologies: From research to application. *Innovation
(Camb)* **3**, 100342 (2022).
- 679 4. Oh, S. W. *et al.* A mesoscale connectome of the mouse brain. *Nature* **508**, 207–14
(2014).
- 680 5. Gong, H. *et al.* Continuously tracing brain-wide long-distance axonal projections in
mice at a one-micron voxel resolution. *Neuroimage* **74**, 87–98 (2013).
- 681 6. Li, A. *et al.* Micro-optical sectioning tomography to obtain a high-resolution atlas of
the mouse brain. *Science* **330**, 1404–8 (2010).
- 682 7. Ueda, H. R. *et al.* Tissue clearing and its applications in neuroscience. *Nat Rev
Neurosci* **21**, 61–79 (2020).
- 683 8. Ståhl, P. L. *et al.* Visualization and analysis of gene expression in tissue sections by
spatial transcriptomics. *Science* **353**, 78–82 (2016).
- 684 9. Burgess, D. J. Spatial transcriptomics coming of age. *Nat Rev Genet* **20**, 317 (2019).
- 685 10. Hardwick, S. A. *et al.* Single-nuclei isoform RNA sequencing unlocks barcoded exon
connectivity in frozen brain tissue. *Nature biotechnology* **40**, 1082–1092 (2022).
- 686 11. Hawrylycz, M. *et al.* A guide to the BRAIN initiative cell census network data
ecosystem. *PLoS biology* **21**, e3002133 (2023).
- 687 12. Wang, Q. *et al.* The allen mouse brain common coordinate framework: A 3D reference
atlas. *Cell* **181**, 936–953.e20 (2020).
- 688 13. Perens, J. *et al.* An optimized mouse brain atlas for automated mapping and quantification
of neuronal activity using iDISCO+ and light sheet fluorescence microscopy.
Neuroinformatics **19**, 433–446 (2021).
- 689 14. Ma, Y. *et al.* A three-dimensional digital atlas database of the adult C57BL/6J mouse
brain by magnetic resonance microscopy. *Neuroscience* **135**, 1203–1215 (2005).

- 690 15. Qu, L. *et al.* Cross-modal coherent registration of whole mouse brains. *Nature Methods* **19**, 111–118 (2022).
- 691 16. Kronman, F. N. *et al.* [Developmental mouse brain common coordinate framework](#). *Nat Commun* **15**, 9072 (2024).
- 692 17. Chuang, N. *et al.* An MRI-based atlas and database of the developing mouse brain. *Neuroimage* **54**, 80–89 (2011).
- 693 18. Dries, R. *et al.* Advances in spatial transcriptomic data analysis. *Genome research* **31**, 1706–1718 (2021).
- 694 19. Ricci, P. *et al.* Removing striping artifacts in light-sheet fluorescence microscopy: A review. *Progress in biophysics and molecular biology* **168**, 52–65 (2022).
- 695 20. Agarwal, N., Xu, X. & Gopi, M. Robust registration of mouse brain slices with severe histological artifacts. in *Proceedings of the tenth indian conference on computer vision, graphics and image processing* 1–8 (2016).
- 696 21. Agarwal, N., Xu, X. & Gopi, M. Automatic detection of histological artifacts in mouse brain slice images. in *Medical computer vision and bayesian and graphical models for biomedical imaging: MICCAI 2016 international workshops, MCV and BAMBI, athens, greece, october 21, 2016, revised selected papers* 8 105–115 (Springer, 2017).
- 697 22. Tward, D. *et al.* 3d mapping of serial histology sections with anomalies using a novel robust deformable registration algorithm. in *International workshop on multimodal brain image analysis* 162–173 (Springer, 2019).
- 698 23. Cahill, L. S. *et al.* Preparation of fixed mouse brains for MRI. *Neuroimage* **60**, 933–939 (2012).
- 699 24. Biancalani, T. *et al.* [Deep learning and alignment of spatially resolved single-cell transcriptomes with tangram](#). *Nat Methods* **18**, 1352–1362 (2021).
- 700 25. Sunkin, S. M. *et al.* Allen brain atlas: An integrated spatio-temporal portal for exploring the central nervous system. *Nucleic acids research* **41**, D996–D1008 (2012).
- 701 26. Kim, Y. *et al.* Brain-wide maps reveal stereotyped cell-type-based cortical architecture and subcortical sexual dimorphism. *Cell* **171**, 456–469 (2017).

- 702 27. Fürth, D. *et al.* An interactive framework for whole-brain maps at cellular resolution. *Nat Neurosci* **21**, 139–149 (2018).
- 703 28. Li, Y. *et al.* mBrainAligner-web: A web server for cross-modal coherent registration of whole mouse brains. *Bioinformatics* **38**, 4654–4655 (2022).
- 704 29. Puchades, M. A., Csucs, G., Ledergerber, D., Leergaard, T. B. & Bjaalie, J. G. Spatial registration of serial microscopic brain images to three-dimensional reference atlases with the QuickNII tool. *PloS one* **14**, e0216796 (2019).
- 705 30. Eastwood, B. S. *et al.* Whole mouse brain reconstruction and registration to a reference atlas with standard histochemical processing of coronal sections. *Journal of Comparative Neurology* **527**, 2170–2178 (2019).
- 706 31. Ni, H. *et al.* A robust image registration interface for large volume brain atlas. *Sci Rep* **10**, 2139 (2020).
- 707 32. Pallast, N. *et al.* Processing pipeline for atlas-based imaging data analysis of structural and functional mouse brain MRI (AIDAmri). *Front Neuroinform* **13**, 42 (2019).
- 708 33. Celestine, M., Nadkarni, N. A., Garin, C. M., Bougacha, S. & Dhenain, M. Sammba-MRI: A library for processing SmAll-MaMmal BrAin MRI data in python. *Front Neuroinform* **14**, 24 (2020).
- 709 34. Ioanas, H.-I., Marks, M., Zerbi, V., Yanik, M. F. & Rudin, M. An optimized registration workflow and standard geometric space for small animal brain imaging. *Neuroimage* **241**, 118386 (2021).
- 710 35. Aggarwal, M., Zhang, J., Miller, M. I., Sidman, R. L. & Mori, S. Magnetic resonance imaging and micro-computed tomography combined atlas of developing and adult mouse brains for stereotaxic surgery. *Neuroscience* **162**, 1339–1350 (2009).
- 711 36. Chandrashekhar, V. *et al.* CloudReg: Automatic terabyte-scale cross-modal brain volume registration. *Nature methods* **18**, 845–846 (2021).
- 712 37. Jin, M. *et al.* SMART: An open-source extension of WholeBrain for intact mouse brain registration and segmentation. *eNeuro* **9**, (2022).
- 713 38. Negwer, M. *et al.* FriendlyClearMap: An optimized toolkit for mouse brain mapping and analysis. *Gigascience* **12**, (2022).

- 714 39. Lin, W. *et al.* Whole-brain mapping of histaminergic projections in mouse brain. *Proceedings of the National Academy of Sciences* **120**, e2216231120 (2023).
- 715 40. Zhang, M. *et al.* Spatially resolved cell atlas of the mouse primary motor cortex by MERFISH. *Nature* **598**, 137–143 (2021).
- 716 41. Shi, H. *et al.* Spatial atlas of the mouse central nervous system at molecular resolution. *Nature* **622**, 552–561 (2023).
- 717 42. Zhang, Y. *et al.* Reference-based cell type matching of *in situ* image-based spatial transcriptomics data on primary visual cortex of mouse brain. *Scientific Reports* **13**, 9567 (2023).
- 718 43. Klein, S., Staring, M., Murphy, K., Viergever, M. A. & Pluim, J. P. W. [Elastix: A toolbox for intensity-based medical image registration](#). *IEEE Trans Med Imaging* **29**, 196–205 (2010).
- 719 44. Fedorov, A. *et al.* 3D slicer as an image computing platform for the quantitative imaging network. *Magnetic resonance imaging* **30**, 1323–1341 (2012).
- 720 45. Tustison, N. J. *et al.* [The ANTsX ecosystem for quantitative biological and medical imaging](#). *Sci Rep* **11**, 9068 (2021).
- 721 46. Yao, Z. *et al.* [A high-resolution transcriptomic and spatial atlas of cell types in the whole mouse brain](#). *Nature* **624**, 317–332 (2023).
- 722 47. Pagani, M., Damiano, M., Galbusera, A., Tsafaris, S. A. & Gozzi, A. Semi-automated registration-based anatomical labelling, voxel based morphometry and cortical thickness mapping of the mouse brain. *Journal of neuroscience methods* **267**, 62–73 (2016).
- 723 48. Anderson, R. J. *et al.* [Small animal multivariate brain analysis \(SAMBA\) - a high throughput pipeline with a validation framework](#). *Neuroinformatics* **17**, 451–472 (2019).
- 724 49. Allan Johnson, G. *et al.* Whole mouse brain connectomics. *Journal of Comparative Neurology* **527**, 2146–2157 (2019).
- 725 50. Avants, B. B., Epstein, C. L., Grossman, M. & Gee, J. C. [Symmetric diffeomorphic image registration with cross-correlation: Evaluating automated labeling of elderly and neurodegenerative brain](#). *Med Image Anal* **12**, 26–41 (2008).

- 726 51. Tustison, N. J. *et al.* N4ITK: Improved N3 bias correction. *IEEE Trans Med Imaging* **29**, 1310–20 (2010).
- 727 52. Bajcsy, R. & Broit, C. Matching of deformed images. in *Sixth International Conference on Pattern Recognition (ICPR'82)* 351–353 (1982).
- 728 53. Bajcsy, R. & Kovacic, S. Multiresolution elastic matching. *Computer Vision, Graphics, and Image Processing* **46**, 1–21 (1989).
- 729 54. Gee, J. C., Reivich, M. & Bajcsy, R. Elastically deforming 3D atlas to match anatomical brain images. *J Comput Assist Tomogr* **17**, 225–36 (1993).
- 730 55. Klein, A. *et al.* Evaluation of 14 nonlinear deformation algorithms applied to human brain MRI registration. *Neuroimage* **46**, 786–802 (2009).
- 731 56. Murphy, K. *et al.* Evaluation of registration methods on thoracic CT: The EMPIRE10 challenge. *IEEE Trans Med Imaging* **30**, 1901–20 (2011).
- 732 57. Baheti, B. *et al.* The brain tumor sequence registration challenge: Establishing correspondence between pre-operative and follow-up MRI scans of diffuse glioma patients. (2021).
- 733 58. Avants, B. B. *et al.* The optimal template effect in hippocampus studies of diseased populations. *Neuroimage* **49**, 2457–66 (2010).
- 734 59. Avants, B. B., Tustison, N. J., Wu, J., Cook, P. A. & Gee, J. C. An open source multivariate framework for n-tissue segmentation with evaluation on public data. *Neuroinformatics* **9**, 381–400 (2011).
- 735 60. Manjón, J. V., Coupé, P., Martí-Bonmatí, L., Collins, D. L. & Robles, M. Adaptive non-local means denoising of MR images with spatially varying noise levels. *J Magn Reson Imaging* **31**, 192–203 (2010).
- 736 61. Wang, H. *et al.* Multi-atlas segmentation with joint label fusion. *IEEE Trans Pattern Anal Mach Intell* **35**, 611–23 (2013).
- 737 62. Tustison, N. J. *et al.* Optimal symmetric multimodal templates and concatenated random forests for supervised brain tumor segmentation (simplified) with ANTsR. *Neuroinformatics* (2014) doi:10.1007/s12021-014-9245-2.

- 738 63. Tustison, N. J., Yang, Y. & Salerno, M. [Advanced normalization tools for cardiac motion correction](#). in *Statistical atlases and computational models of the heart - imaging and modelling challenges* (eds. Camara, O. et al.) vol. 8896 3–12 (Springer International Publishing, 2015).
- 739 64. McCormick, M., Liu, X., Jomier, J., Marion, C. & Ibanez, L. [ITK: Enabling reproducible research and open science](#). *Front Neuroinform* **8**, 13 (2014).
- 740 65. Beg, M. F., Miller, M. I., Trouvé, A. & Younes, L. [Computing large deformation metric mappings via geodesic flows of diffeomorphisms](#). *International Journal of Computer Vision* **61**, 139–157 (2005).
- 741 66. Tustison, N. J. & Avants, B. B. [Explicit B-spline regularization in diffeomorphic image registration](#). *Front Neuroinform* **7**, 39 (2013).
- 742 67. Hsu, L.-M. *et al.* CAMRI mouse brain MRI data.
- 743 68. Reshetnikov, V. *et al.* High-resolution MRI data of brain C57BL/6 and BTBR mice in three different anatomical views.
- 744 69. Rahman, N., Xu, K., Budde, M. D., Brown, A. & Baron, C. A. [A longitudinal microstructural MRI dataset in healthy C57Bl/6 mice at 9.4 tesla](#). *Sci Data* **10**, 94 (2023).
- 745 70. Liu, J. *et al.* [Concordance of MERFISH spatial transcriptomics with bulk and single-cell RNA sequencing](#). *Life Sci Alliance* **6**, (2023).
- 746 71. Stringer, C., Wang, T., Michaelos, M. & Pachitariu, M. [Cellpose: A generalist algorithm for cellular segmentation](#). *Nat Methods* **18**, 100–106 (2021).
- 747 72. Jia, H., Yap, P.-T., Wu, G., Wang, Q. & Shen, D. Intermediate templates guided groupwise registration of diffusion tensor images. *NeuroImage* **54**, 928–939 (2011).
- 748 73. Tang, S., Fan, Y., Wu, G., Kim, M. & Shen, D. RABBIT: Rapid alignment of brains by building intermediate templates. *NeuroImage* **47**, 1277–1287 (2009).
- 749 74. Dewey, B. E., Carass, A., Blitz, A. M. & Prince, J. L. Efficient multi-atlas registration using an intermediate template image. in *Proceedings of SPIE—the international society for optical engineering* vol. 10137 (NIH Public Access, 2017).

- 750 75. Perens, J. *et al.* Multimodal 3D mouse brain atlas framework with the skull-derived coordinate system. *Neuroinformatics* **21**, 269–286 (2023).
- 751 76. Rotolo, T., Smallwood, P. M., Williams, J. & Nathans, J. Genetically-directed, cell type-specific sparse labeling for the analysis of neuronal morphology. *PLoS One* **3**, e4099 (2008).
- 752 77. Peng, H. *et al.* Morphological diversity of single neurons in molecularly defined cell types. *Nature* **598**, 174–181 (2021).
- 753 78. Gong, H. *et al.* High-throughput dual-colour precision imaging for brain-wide connectome with cytoarchitectonic landmarks at the cellular level. *Nat Commun* **7**, 12142 (2016).
- 754 79. Wang, J. *et al.* Divergent projection patterns revealed by reconstruction of individual neurons in orbitofrontal cortex. *Neurosci Bull* **37**, 461–477 (2021).
- 755 80. Avants, B. B. *et al.* The Insight ToolKit image registration framework. *Front Neuroinform* **8**, 44 (2014).
- 756 81. Chon, U., Vanselow, D. J., Cheng, K. C. & Kim, Y. Enhanced and unified anatomical labeling for a common mouse brain atlas. *Nat Commun* **10**, 5067 (2019).
- 757 82. Tasic, B. *et al.* Adult mouse cortical cell taxonomy revealed by single cell transcriptomics. *Nat Neurosci* **19**, 335–46 (2016).
- 758 83. Bergmann, E., Gofman, X., Kavushansky, A. & Kahn, I. Individual variability in functional connectivity architecture of the mouse brain. *Commun Biol* **3**, 738 (2020).
- 759 84. Billot, B. *et al.* SynthSeg: Segmentation of brain MRI scans of any contrast and resolution without retraining. *Med Image Anal* **86**, 102789 (2023).
- 760 85. Rolfe, S. M., Whikehart, S. M. & Maga, A. M. Deep learning enabled multi-organ segmentation of mouse embryos. *Biol Open* **12**, bio059698 (2023).
- 761 86. Tustison, N. J. & Gee, J. C. Generalized n -d C^k B-spline scattered data approximation with confidence values. in *Medical imaging and augmented reality* (eds. Yang, G.-Z., Jiang, T., Shen, D., Gu, L. & Yang, J.) 76–83 (Springer Berlin Heidelberg, 2006).
- 762 87. Falk, T. *et al.* U-net: Deep learning for cell counting, detection, and morphometry. *Nat Methods* **16**, 67–70 (2019).

- ⁷⁶³ 88. Isensee, F., Jaeger, P. F., Kohl, S. A. A., Petersen, J. & Maier-Hein, K. H. [nnU-net: A self-configuring method for deep learning-based biomedical image segmentation.](#) *Nat Methods* **18**, 203–211 (2021).
- ⁷⁶⁴ 89. Tustison, N. J. *et al.* Image- versus histogram-based considerations in semantic segmentation of pulmonary hyperpolarized gas images. *Magn Reson Med* **86**, 2822–2836 (2021).

⁷⁶⁵ **Acknowledgments**

⁷⁶⁶ Support for the research reported in this work includes funding from the National Institute
⁷⁶⁷ of Biomedical Imaging and Bioengineering (R01-EB031722) and National Institute of Mental
⁷⁶⁸ Health (RF1-MH124605, U24-MH114827, and NIH RF1MH124605 to Y.K.).

⁷⁶⁹ We also acknowledge the data contribution of Dr. Adam Raikes (GitHub @araikes) of the
⁷⁷⁰ Center for Innovation in Brain Science at the University of Arizona for refining the weights
⁷⁷¹ of the mouse brain extraction network.

⁷⁷² **Author contributions**

⁷⁷³ N.T., M.C., and J.G. wrote the main manuscript text and figures. M.C., M.K., R.D., S.S.,
⁷⁷⁴ Q.W., L.G., J.D., C.G., and J.G. developed the Allen registration pipelines. N.T., F.K.,
⁷⁷⁵ J.G., and Y.K. developed the time-varying velocity transformation model for the DevCCF.
⁷⁷⁶ N.T. and M.T. developed the brain parcellation and cortical thickness methodology. All
⁷⁷⁷ authors reviewed the manuscript.

⁷⁷⁸ Competing Interests

⁷⁷⁹ The authors declare no competing interests.

Tables

Table 1: Sampling of ANTsX functionality

ANTsPy: Preprocessing	
bias field correction	<code>n4_bias_field_correction(...)</code>
image denoising	<code>denoise_image(...)</code>
ANTsPy: Registration	
intensity image registration	<code>registration(...)</code>
label image registration	<code>label_image_registration(...)</code>
image transformation	<code>apply_transforms(...)</code>
template generation	<code>build_template(...)</code>
landmark registration	<code>fit_transform_to_paired_points(...)</code>
time-varying landmark reg.	<code>fit_time_varying_transform_to_point_sets(...)</code>
integrate velocity field	<code>integrate_velocity_field(...)</code>
invert displacement field	<code>invert_displacement_field(...)</code>
ANTsPy: Segmentation	
MRF-based segmentation	<code>atropos(...)</code>
Joint label fusion	<code>joint_label_fusion(...)</code>
diffeomorphic thickness	<code>kelly_kapowski(...)</code>
ANTsPy: Miscellaneous	
Regional intensity statistics	<code>label_stats(...)</code>
Regional shape measures	<code>label_geometry_measures(...)</code>
B-spline approximation	<code>fit_bspline_object_to_scattered_data(...)</code>
Visualize images and overlays	<code>plot(...)</code>
<i>ANTsPyNet: Mouse-specific</i>	
brain extraction	<code>mouse_brain_extraction(...modality="t2"...)</code>
brain parcellation	<code>mouse_brain_parcellation(...)</code>
cortical thickness	<code>mouse_cortical_thickness(...)</code>
super resolution	<code>mouse_histology_super_resolution(...)</code>

ANTsX provides state-of-the-art functionality for processing biomedical image data. Such tools, including deep learning networks, support a variety of mapping-related tasks. A more comprehensive listing of ANTsX tools with self-contained R and Python examples is provided as a gist page on GitHub (<https://tinyurl.com/antsxtutorial>).

781 **Figure Legends**

782 **Figure 1.** Diagram of the two ANTsX-based pipelines for mapping (a) MERFISH and
783 (b)fMOST data into the space of AllenCCFv3. Each generates the requisite transforms to
784 map individual images to the CCF.

785 **Figure 2.** The spatial transformation between any two time points within the continu-
786 ous DevCCF longitudinal developmental trajectory is available through the use of ANTsX
787 functionality for generating a velocity flow model.

788 **Figure 3.** Annotated regions representing common labels across developmental stages,
789 shown for both P4 and P14.

790 **Figure 4.** Convergence and evaluation of the velocity flow model across the DevCCF
791 develop- mental trajectory. (Top left) Total displacement error over iterations. (Top right)
792 Median displacement error per integration point across the optimization timeline, spanning
793 embryonic (E11.5) to postnatal (P56) stages. (Bottom) Dice similarity scores comparing
794 region-level label overlap between: (1) conventional pairwise SyN registration and (2) ve-
795 locity flow-based deformation, across intermediate timepoints. Using region-based pairwise
796 registration with SyN as a performance upper bound, the velocity flow model achieves com-
797 parable accuracy while also enabling smooth, continuous deformation across the full devel-
798 opmental continuum.

799 **Figure 5.** Mid-sagittal visualization of DevCCF templates warped to every other time
800 point. Each row is a reference space; each column is a warped input. Diagonal entries show
801 original templates.

802 **Figure 6.** Example of generating “virtual” DevCCF templates at intermediate time points
803 (e.g., P10.3, P20) by warping adjacent stages to a shared time and averaging using ANTsX.

804 **Figure 7.** The mouse brain cortical labeling pipeline integrates two deep learning compo-
805 nents for brain extraction and anatomical region segmentation. Both networks rely heavily
806 on data augmentation applied to templates constructed from open datasets. The framework
807 also supports further refinement or alternative label sets tailored to specific research needs.
808 Possible applications include voxelwise cortical thickness estimation.

809 **Figure 8.** Evaluation of the ANTsX mouse brain extraction on an independent, publicly
810 available dataset consisting of 12 specimens \times 7 time points = 84 total images. Dice overlap
811 comparisons with the user-generated brain masks provide good agreement with the auto-
812 mated results from the brain extraction network.

813 **Figure 9.** Evaluation of the ANTsX deep learning-based mouse brain parcellation on a
814 diverse MRI cohort. (a) T2-weighted DevCCF P56 template with the six-region parcella-
815 tion: cerebral cortex, nuclei, brain stem, cerebellum, main olfactory bulb, and hippocampal
816 formation. (b) Example segmentation result from a representative subject (NR5, Day 0)
817 using the proposed deep learning pipeline. (c) Dice overlap scores across the full evaluation
818 cohort ($n = 84$), comparing anatomical alignment achieved via registration using intensity
819 alone versus registration guided by the predicted parcellation. Dice values were computed
820 using manually segmented labels transformed to AllenCCFv3 space.